Applied Catalysis B: Environmental 228 (2018) 10–18

Contents lists available at ScienceDirect

Applied Catalysis B: Environmental

journal homepage: www.elsevier.com/locate/apcatb

Boosting photocatalytic water oxidation reactions over strontium tantalum oxynitride by structural laminations

Shunhang Wei, Xiaoxiang Xu*

Shanghai Key Lab of Chemical Assessment and Sustainability, School of Chemical Science and Engineering, Tongji University, 1239 Siping Road, Shanghai, 200092, China

ARTICLE INFO

Keywords:
$SrTaO_2N$
Sr_2TaO_3N
Water splitting
Photocatalyst
Oxygen production

ABSTRACT

Perovskite oxynitrides often own a poor photocatalytic activity under normal conditions, being incommensurate to their strong visible light absorbance. This is particularly true for $SrTaO_2N$ which undergoes self-oxidative decompositions even under protection of a hole scavenger. In this work, we laminate the crystal structure of $SrTaO_2N$ by inserting extra layers of SrO to form a Ruddlesden-Popper (RP) compound Sr_2TaO_3N. This structural modification not only improves the light absorption of $SrTaO_2N$ but also effectively suppresses the defect formation such as Ta^{4+} species etc. More importantly, Sr_2TaO_3N is able to drive photocatalytic water oxidation reactions under visible light illumination ($\lambda \geq 420$ nm) without the aid of a cocatalyst and self-oxidative decompositions found for $SrTaO_2N$ are largely inhibited. Further analysis suggests that the presence of extra SrO layers positively shifts the valence band edge and stabilizes N species in the structure according to Pauling's second rule. Theoretical calculations indicate that Sr_2TaO_3N has typical 2D charge transportation properties which are associated with the structural laminations. Its conduction band minimum (CBM) and valence band maximum (VBM) are found to be located within TaN_2O_2 square planes which favors efficient charge transportations.

1. Introduction

The fossil-fuel based economy of our modern society is essentially not sustainable, not only because of a rapid depletion of fossil fuel reservoirs but also from environmental considerations [1–4]. An attractive strategy to release us from fossil fuel reliance is to build a hydrogen-based energy infrastructure that is clean and renewable without sacrifice from environmental degradations [5,6]. Photocatalytic water splitting into hydrogen and oxygen on particulate semiconductors, driven by solar insolation, offers an ideal scenario to this strategy as water is a recyclable product of hydrogen and solar energy is inexhaustible in nature and widely accessible all over the world [7–19]. However, most semiconductor photocatalysts that are thermodynamically viable for water splitting own a band gap too large to fit the solar spectral range, being inappropriate for this purpose [20–22]. More importantly, complete water splitting is generally hampered by the sluggish water-oxidation reactions which involve the participation of four holes and four electrons and are energetically and mechanistically cumbersome [23–27]. Therefore, searching/developing photocatalytic materials/systems that are sensitive to a large portion of solar photons as well as active to water-oxidation reactions is a prerequisite to realize solar hydrogen production from water. In this regard, great attention has been paid to metal nitrides and oxynitrides not only because of their proper band gap ($\sim$ 2.0 eV) that can harness a significant portion of solar spectrum but also due to their intriguing photocatalytic activity towards water oxidation [28–31]. For instance, Ta_3N_5 is sensitive to photons as far as 600 nm and exhibit superior efficiency for oxygen production from water under appropriate conditions [24,32,33]. Nevertheless, a number of perovskite oxynitrides ($LaTiO_2N$ [34,35], AMO_2N (A = Ca, Sr and Ba; M = Nb and Ta) [29,36–38], $LaMON_2$ (M = Nb and Ta) [39]) demonstrate poor photocatalytic activities under normal conditions, being incommensurate to their substantial visible light absorption. Interfacial or bulk defects produced during material synthesis (high temperature and in the presence of ammonia) are believed to be responsible for their poor performance [34,40–42]. Recent efforts on defects management by doping or interfacial treatment have gained some success in improving their photocatalytic performance yet still bear the risks of introducing additional defects which might be detrimental to the activity [24,26,27,43]. In this work, we developed a new method to improve the photocatalytic performance of perovskite oxynitrides by structural laminations, i.e. inserting extra layers of SrO into $SrTaO_2N$ to form Ruddlesden-Popper (RP) compound Sr_2TaO_3N. $SrTaO_2N$ generally owns the poorest photocatalytic activity among perovskite series

* Corresponding author.
E-mail address: xxxu@tongji.edu.cn (X. Xu).

https://doi.org/10.1016/j.apcatb.2018.01.071
Received 17 November 2017; Received in revised form 26 January 2018; Accepted 29 January 2018
Available online 31 January 2018

$ATaO_2N$ (A = Ca, Sr and Ba) [36] and is suffered by self-oxidative decomposition even under the protection of an electron donor [37,38]. Laminating the crystal structure of $SrTaO_2N$ substantially extends its light absorption, reduces the defect levels, stabilizes the compound and boosts the photocatalytic oxygen production from water.

2. Experimental

2.1. Material synthesis

$SrTaO_2N$ and its laminated counterpart Sr_2TaO_3N were synthesized by nitridizing appropriate metal oxide precursors. These precursors were prepared by standard polymerized complex (PC) method: proper amounts of strontium nitrate (SCR, 99.5%), tantalum pentachloride (Aladdin, 99.99%), citric acid (Aladdin, 99.5%) and ethylene glycol (Aladdin, GC grade) were dissolved in 5 mL anhydrous ethanol (Aladdin, 99.9%) to form a transparent solution. The solution was magnetically stirred at 423 K for 3 h and 573 K for another 3 h to promote polymerization. The resultant brown resin was transferred into alumina crucibles and calcined at 823 K for 20 h in order to remove organic species. White powders were produced after calcination and were further nitridized in a tube furnace. The nitridation was performed at 1273 K for 20 h under continuous flow of ultrapure ammonia gas (Jiaya Chemicals, 99.999%). Typical gas flow rate was set at 400 mL min^{-1}.

2.2. Materials characterization

Phase purity and crystal structure of sample powders were examined by X-ray powder diffraction (XRD) techniques on a Bruker D8 Focus diffractometer. Incident X-ray radiation were Cu $K_{\alpha1}$ (λ = 1.5406 Å) and Cu $K_{\alpha2}$ (λ = 1.5444 Å). Typical step size for signal collection was 0.01° and a duration time of 10 s at each step. Crystal structure analysis and simulation was performed using General Structure Analysis System (GSAS) software package for Rietveld refinement [44]. The morphology of the samples was inspected under a field emission scanning electron microscope (Hitachi S4800) and a transmission electron microscope (JEOL JEM-2100). Diffuse reflectance spectra were collected using a UV–vis spectrometer (JASCO-V750) and were analyzed using JASCO software suite. $BaSO_4$ was used as a non-absorbing reference material. Surface state of sample powders was analyzed by X-ray photoelectron spectroscopy (XPS) technique (AXIS Ultra DLD, monochromatic Al K_α X-ray source). All binding energies were adjusted according to adventitious C 1s peak (284.7 eV) [45]. The nitrogen content in sample powders was determined by thermogravimetric analysis (TGA) (SETARAM, Labsys evo DSC). Surface areas were examined by using a Micromeritics instrument TriStar 3000 and were calculated using the Brunauer-Emmett-Teller (BET) model. Mott-Schottky analysis was performed on a Zahner electrochemical workstation with a three-electrode configuration setup. The working electrode was fabricated by electrophoretic deposition method: two pieces of fluorine doped tin oxide (FTO) glass (30 × 10 mm) were immersed in 50 ml acetone solution containing 40 mg sample powders and 10 mg iodine. The two pieces of glass were kept in parallel to each other with a separation distance of 10 mm and conductive sides faced inward. A constant bias (30 V) was applied to the pair of glass for 3 min under potentiostatic control (Keithley 2450 Source Meter). The prepared electrode was then calcined at 473 K in air for 10 min to remove absorbed iodine. Pt foil (10 × 10 mm) and Ag/AgCl electrode were used as counter and reference electrodes respectively. Aqueous K_3PO_4/K_2HPO_4 (0.1 M, pH = 7.95) solution was used as an electrolyte and a buffer.

2.3. Photocatalytic activity

Photocatalytic activities of freshly prepared samples were evaluated by monitoring the O_2 evolution in the presence of sacrificial agent under visible light illumination ($\lambda \geq$ 420 nm). The experiments were carried out in a top-irradiation-type reactor connected to a gas closed circulation and evacuation system (Perfect Light, Labsolar-IIIAG). In a typical experiment, 50 mg sample powders was dispersed into a 100 mL silver nitrate aqueous solution (0.025 M) containing 50 mg La_2O_3. The suspension was then sealed in the reactor and subjected to evacuation for the removal of gas dissolved. Silver nitrate (0.025 M) or sodium persulfate (0.05 M) aqueous solution was used as an electron scavenger to promote the water oxidation reactions and La_2O_3 was introduced to control the pH of the solution. CoO_x was used as a cocatalyst to facilitate water oxidation reactions and was loaded onto sample powders by simply mixing method: proper amounts of CoO were ground with sample powders and the admixtures were calcined at 673 K in N_2 for 1 h. SEM-EDS and TEM analysis confirms the homogeneous distribution and firm anchorage of CoO_x onto the surface of sample powders (Fig. S5). A 300 W Xeon lamp (Perfect Light, PLX-SXE300) was used as the light source, which is coupled with a UV cutoff filter ($\lambda \geq$ 420 nm) to generate visible light. Water jacket was used to stabilize the reactor temperature around 293 K. The gas within the reactor was sampled by an on-line gas chromatograph (TECHCOMP, GC7900) containing a thermal conductivity detector (TCD) (5 Å molecular sieve columns and Ar carrier gas).

2.4. Theoretical calculations

Theoretical calculations were carried out using density functional theory (DFT) which is implemented through the Vienna Ab initio Simulation Package (VASP) [46]. The Perdew, Burke and Ernzerhof (PBE) exchange-correlation functional within the generalized gradient approxiamtion (GGA) [47] and the projector augmented-wave pseudopotential were applied for calculations [48]. A 2 × 2 × 1 supercell ($a = b$ = 8.1 Å, c = 12.6 Å, $\alpha = \beta = \gamma$ = 90°) with tetragonal symmetry was built for simulation of Sr_2TaO_3N. N atoms were set to be randomly located at the equatorial positions of TaO_4N_2 octahedrons with *cis*-type arrangements. All geometry structures were fully relaxed until the forces on each atom are less than 0.01 eV/Å. Static calculations were done with a 7 × 7 × 4 Monkhorst-Pack *k*-point grid [49].

3. Results and discussions

3.1. Phase purity and crystal structure

The crystal structure of perovskite metal oxynitrides AMX_3 (A = Ca, Sr, Ba, La and Eu; M = Nb, Ta and Zr; X = N/O) has been an intriguing topic for both experimental and theoretical studies [50]. A wealth of important properties such as optical, photocatalytic, dielectric and magnetoresistive properties etc. have been found to be strongly correlated with local anion ordering within the perovskite lattice [51–54]. The general findings are the covalency driven *cis*-type arrangement of N in MX_6 octahedrons and the formation of disordered zigzag -M-N-chains along perovskite network [50]. This leads to the segregation of N atoms into two-dimensional (2D) planes within the perovskite lattice for $SrTaO_2N$ where inequivalent O and $O_{0.5}N_{0.5}$ anion sites appear in the *ab* plane. An orthorhombic supercell ($2a_p \times 2a_p \times 2a_p$) with space group *Fmmm* is found to be most appropriated to describe the crystal structure of $SrTaO_2N$ (Glazer notion $a^{\circ}b^{\circ}c^{-}$) [55]. Our Rietveld refinement using space group *Fmmm* converges with better *R*-factors and χ^2 (R_p = 4.18%, R_{wp} = 5.67%, χ^2 = 1.456) compared to those using space group *I4mcm* (R_p = 6.05%, R_{wp} = 4.50%, χ^2 = 1.654) (Fig. S1) which has been adopted by other research groups [56,57]. The refined unit cell parameters are tabulated in Table 1. The inequivalent O and $O_{0.5}N_{0.5}$ anion sites within $SrTaO_2N$ structure can be easily distinguished (Fig. 1a). Previous report has pointed out that such a *cis*-type configuration in MX_6 octahedrons origins from the high tendency for d° transition metal ions to maximize $M(d_\pi)$-$X(p_\pi)$ covalency (here $Ta(5d_\pi)$-

Table 1
Unit cell parameters, BET surface area and band gap values of freshly prepared $SrTaO_2N$ and Sr_2TaO_3N, standard deviation in the parenthesis.

	Space group	a/Å	b/Å	c/Å	V/Å^3	BET surface area/m^2/g	Band gap/eV
$SrTaO_2N$	*Fmmm*	8.0638 (6)	8.0524 (6)	8.0798 (4)	524.66 (3)	5.4 (1)	2.13 (2)
Sr_2TaO_3N	*I4/mmm*	4.0448 (2)	4.0448 (2)	12.6002 (7)	206.15 (3)	0.2 (1)	1.97 (2)

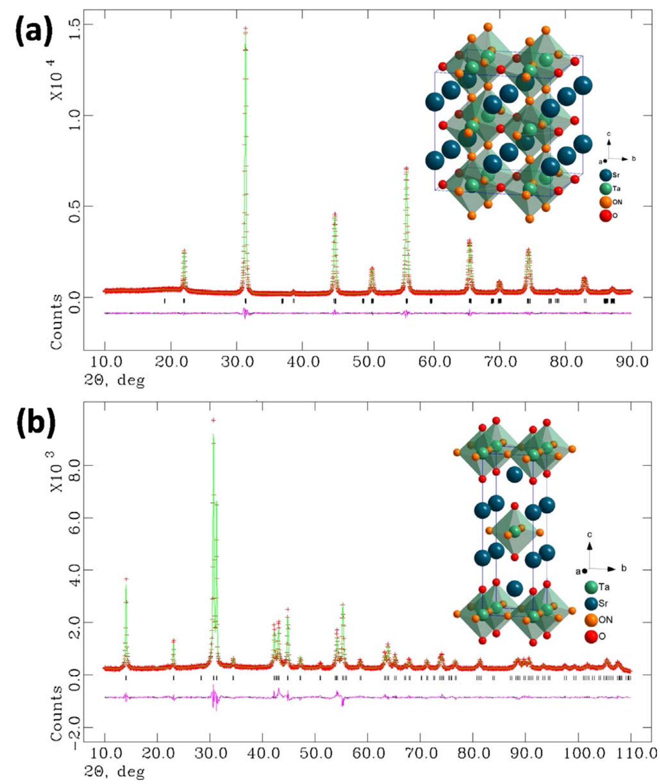

Fig. 1. Observed and calculated X-ray powder diffraction patterns of as-prepared samples: (a) $SrTaO_2N$ (the refinement converges with R_p = 4.18%, R_{wp} = 5.67%, χ^2 = 1.456) and (b) Sr_2TaO_3N (the refinement converges with R_p = 6.18%, R_{wp} = 7.89%, χ^2 = 2.539), schematic representations of refined crystal structures are illustrated in the inserted images.

N($2p_\pi$)) [50,58]. Nevertheless, Pauling's second rule suggests that summation of electrostatic bond strength of all cations bonded to an anion must be approximately equal to the anion charge (Eq. (1)) [59]:

$$\xi = \sum_i s_i = \sum_i \frac{z_i}{v_i} \tag{1}$$

where ξ is electric charge of the anion, s_i is the electrostatic bond strength of a given cation bonded to the anion, z_i is the charge of cation and v_i is the cation coordination number. The sum of electrostatic bond strength for all anion sites in $SrTaO_2N$ equals to 2.33, which is substantially deviated from charge of nitrogen (3.0). Such a large deviation might be the reason for the instability of $SrTaO_2N$ during photocatalytic water oxidation reactions where large amounts of nitrogen are released due to self-decomposition of $SrTaO_2N$ [26]. In case of Sr_2TaO_3N, our refinement using space group *I4/mmm* gives reasonable fit, being consistent with previous results [60–62]. The preferentially accommodation of N at the equatorial position of TaO_4N_2 octahedrons can be clearly identified (Fig. 1b, inserted image). A simple calculation of electrostatic bond strength for equatorial anion site gives a value of 2.55, being much larger than the one for apical anion site (1.94). Thereby, such a geometrical arrangement of anions in Sr_2TaO_3N (N at equatorial sites and apical sites contain only O) shall have a higher stability compared to the situation in $SrTaO_2N$ according to Pauling's second rule [59]. More interestingly, the crystal structure of Sr_2TaO_3N can be viewed as insertion of extra SrO layers into $SrTaO_2N$ along b direction and concomitant disconnection of TaO_4N_2 octahedrons. The presence of extra layer of SrO as well as structural lamination shall have profound influences on the electronic structure of Sr_2TaO_3N, which will be discussed in the following sections.

3.2. Microstructures

The microstructures of as-prepared $SrTaO_2N$ and Sr_2TaO_3N powders were then examined under field emission scanning electron microscopy (FESEM) and transmission electron microscopy (TEM) conditions. $SrTaO_2N$ powders generally contain small granules with size up to 50 nm (Fig. 2a). These granules tend to agglomerate into large particles and contribute to the relatively small BET surface area observed (Fig. 2b and Table 1). On the contrary, Sr_2TaO_3N powders exhibit bulky particles with size as large as several microns. Close inspection on single particle reveal laminated textures with large amounts of pinholes. These microstructures properly reflect the crystal structures of RP type perovskite compound Sr_2TaO_3N. The large bulky particles in Sr_2TaO_3N are responsible for its much smaller BET surface area than $SrTaO_2N$ (Table 1). High resolution TEM images of Sr_2TaO_3N gives more detailed information on the structural lamination (Fig. 3a and b). Much large separation of lattice fringes (~ 0.63 nm) are clearly identified which corresponds well to the (002) plane of Sr_2TaO_3N.

3.3. UV-Vis spectroscopy

More interestingly, as-prepared $SrTaO_2N$ and Sr_2TaO_3N powders are slightly dissimilar in colors. $SrTaO_2N$ generally owns a yellowish-red color whilst Sr_2TaO_3N are bright red. This is revealed by their UV–vis absorption spectra in which differences in light absorption across the whole spectrum range can be identified (Fig. 4a). There are three major differences: first, light absorption for short-wavelength photons (300 nm ≤ λ ≤ 550 nm) is significantly higher in Sr_2TaO_3N than $SrTaO_2N$. Therefore, Sr_2TaO_3N is expected to be more efficient in absorbing short-wavelength photons which in turn, owns a shorter absorption depth as well as shorter charge migration pathways for photo-generated electrons/holes according to Beer-Lambert Law. Second, the absorption edge is clearly red-shifted in Sr_2TaO_3N compared to $SrTaO_2N$, approaching photon wavelength as far as 700 nm. This is extremely beneficial for photocatalysis as more photons in solar spectrum are eligible to drive the energy-uphill water cleavage reactions. Further calculations based on Kulbelka-Munk transformation of diffuse reflectance data suggest a band gap value of 1.97 eV for Sr_2TaO_3N, which is almost 0.2 eV smaller than $SrTaO_2N$ (Fig. 4b). Third, the absorption tail above 650 nm is considerably depressed in Sr_2TaO_3N with regard to $SrTaO_2N$, being responsible for the bright tone of the red color. Previous studies have pointed out that this absorption tail is generally associated with various types of defects which are detrimental to the photocatalytic activities [23,24,34,63]. Therefore, simply incorporating extra layers of SrO and laminating the crystal structure of $SrTaO_2N$, we have not only gained more light absorption but also managed to control the defects levels inside the perovskite compound. The underlying mechanism for these improvements are not clear but might be explained by the inductive effect of Sr [64]: Sr is much more electropositive or electron donating than Ta [65], therefore, accumulating large amounts of Sr in the structure helps to increase the level of covalency between Ta and N/O, which in turn, favors a small band gap

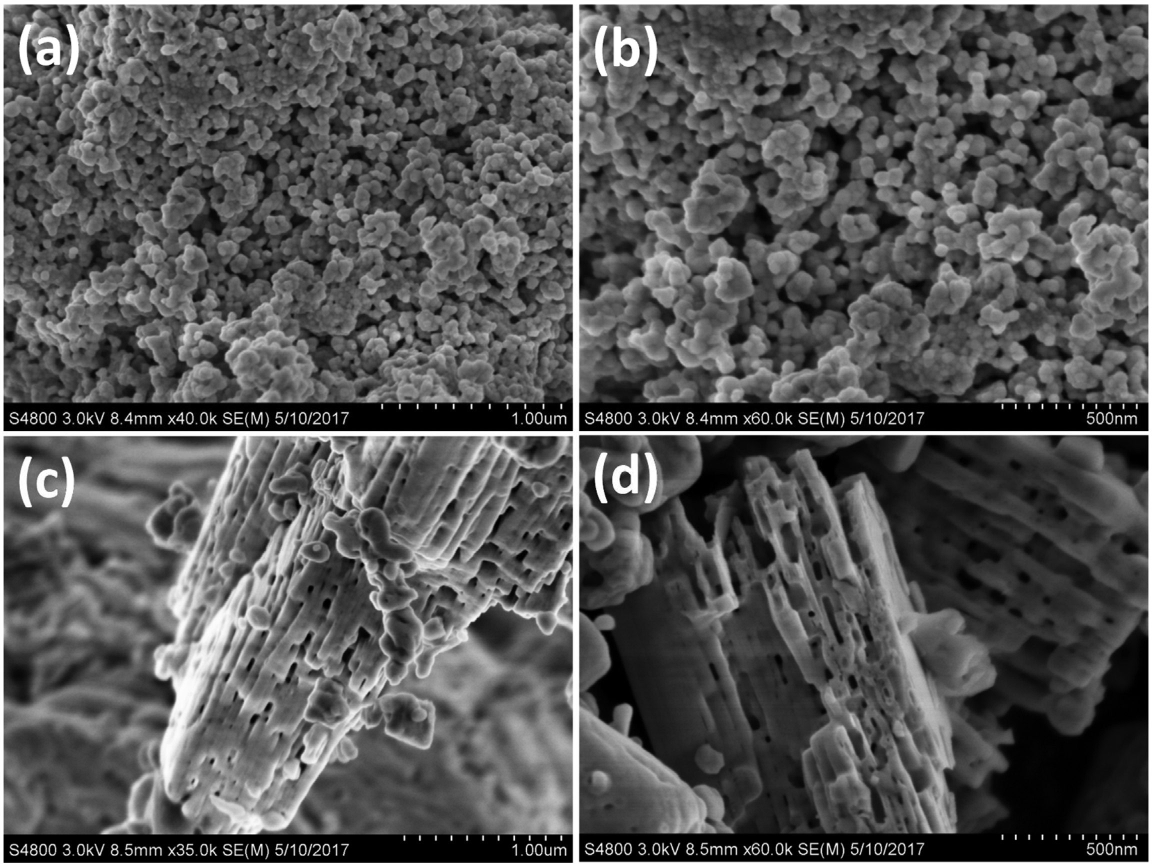

Fig. 2. Field emission scanning electron microscopy images of freshly prepared sample powders: (a) and (b) $SrTaO_2N$, (c) and (d) Sr_2TaO_3N, respectively.

and stabilizes Ta^{5+} and N^{3-}/O^{2-} in the structure (suppress defects such as Ta^{4+}, nitrogen/oxygen vacancies etc.).

3.4. X-ray photoelectron spectroscopy (XPS)

The surface conditions of both $SrTaO_2N$ and Sr_2TaO_3N were further examined using XPS techniques to clarify the role of extra SrO layers to the perovskite compound. Binding energies of core-level electrons of all constituent elements are displayed in Fig. 5. Overlapping peaks are unfolded by applying different Gaussian-Lorentian functions. O 1*s* state for both compounds involves two overlapping peaks centered at 529.8 eV and 531.5 eV which are typical signals for lattice oxygen (O^{2-}) and surface hydroxyl groups (OH^-) [16,17,19,66–71]. It is clear that Sr_2TaO_3N has a much stronger signal for hydroxyl groups than $SrTaO_2N$ which outweighs the one for lattice oxygen. Thereby, the surface of Sr_2TaO_3N is enriched with large amounts of OH groups and is much more hydrophilic compared with $SrTaO_2N$. This property is crucial to the photocatalytic reactions as surface OH groups are frequently involved in the photo-reduction/oxidation steps [72–75]. For Ta 4*f* state, $SrTaO_2N$ displays a broad band which can be separated into four overlapping peaks centered at 24.6 eV, 25.7 eV, 26.6 eV and 27.5 eV, assignable to $4f_{5/2}$ and $4f_{7/2}$ state of Ta^{4+} and Ta^{5+} species [76,77]. The presence of Ta^{4+} in $SrTaO_2N$ is consistent with the high absorption tail in UV–vis spectra [24,27]. On the contrary, only Ta^{5+} signals are found for Sr_2TaO_3N, highlighting the effectiveness of extra SrO layers in stabilizing Ta^{5+} species in the perovskite structure. The N

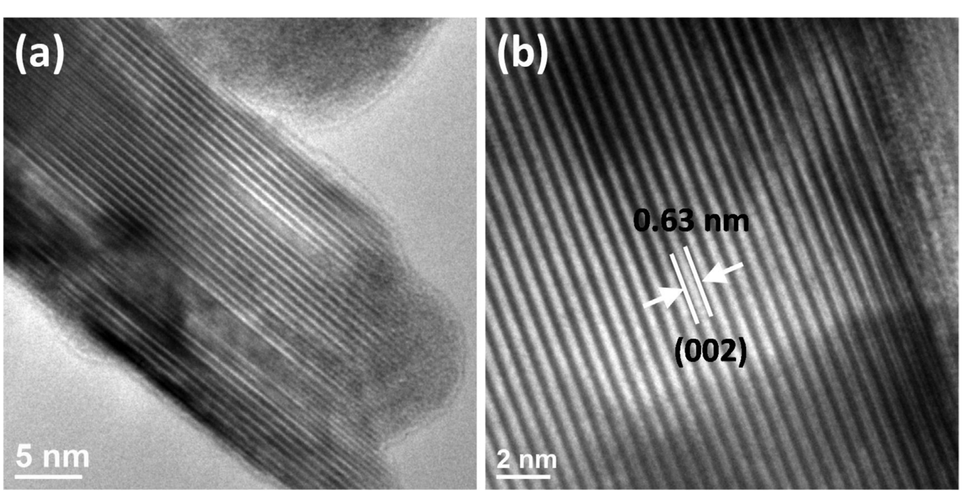

Fig. 3. High resolution transmission electron microscopy images of Sr_2TaO_3N, its layered architectures can be identified from the large separations of lattice fringe which corresponds to (002) plane.

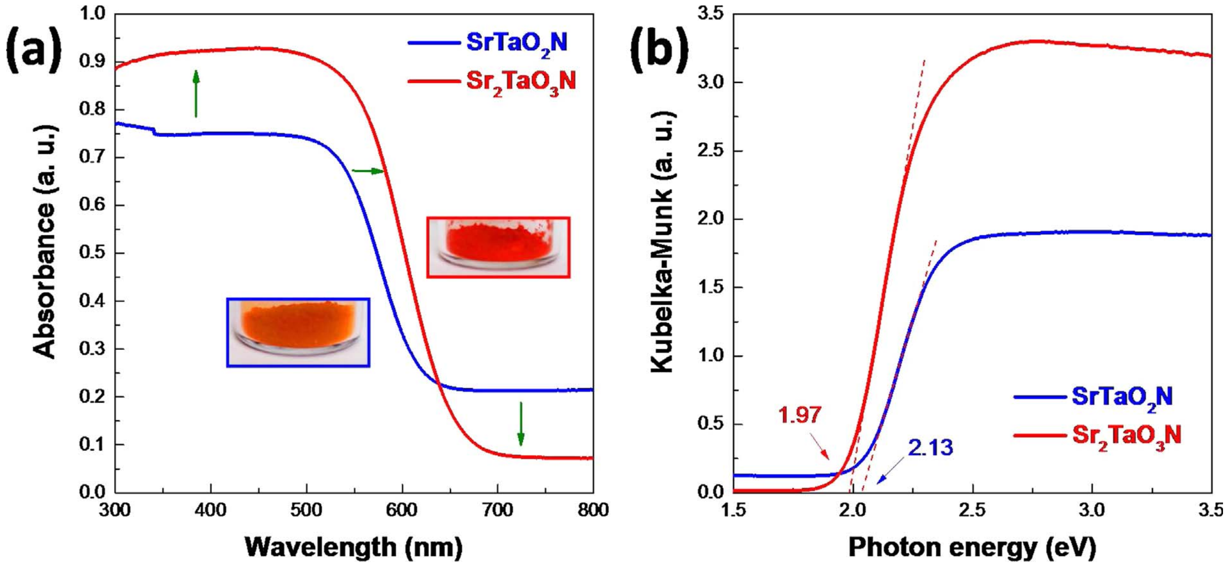

Fig. 4. (a) UV–vis absorption spectra (converted from diffuse reflectance spectra) of as-prepared $SrTaO_2N$ and Sr_2TaO_3N and (b) Kubelka-Munk transformation of diffuse reflectance data, digital photographs of sample powders are inserted for visual inspections. (For interpretation of the references to colour in the text, the reader is referred to the web version of this article.)

1*s* state for both compound shows only a single peak centered at 395.6 eV and is attributed to the lattice nitrogen (N^{3-}) species [78]. Apparently, Sr_2TaO_3N gives a much weaker N 1*s* signal than $SrTaO_2N$, probably due to the relatively lower nitrogen content in the structure. In additional, Sr 3*d* state exhibits two peaks centered around 133.1 eV and 134.8 eV, assignable to Sr $3d_{5/2}$ and Sr $3d_{3/2}$ signals of Sr^{2+} species due to spin-orbital interactions [45,79]. It is worth mentioning that the binding energy of Sr 3*d* state is slightly shifted towards high energy in Sr_2TaO_3N compared to $SrTaO_2N$, probably due to a lower coordination number of Sr in Sr_2TaO_3N (CN = 9) than in $SrTaO_2N$ (CN = 12).

3.5. Photocatalytic water oxidation

Previous reports have suggested that pristine $SrTaO_2N$ is a poor photocatalyst for water splitting despite that it has a strong visible light absorption as far as 600 nm [36–38]. Severe self-oxidative decomposition occurs for $SrTaO_2N$ under conventional photocatalytic conditions even under protection of a hole-scavenger [36–38]. Proper surface engineering and large electrical bias are generally needed for water oxidation reactions on $SrTaO_2N$ [80]. In our case, using $AgNO_3$ as a hole-scavenger and 2.0 wt% CoO_x as a cocatalyst, $SrTaO_2N$ gave

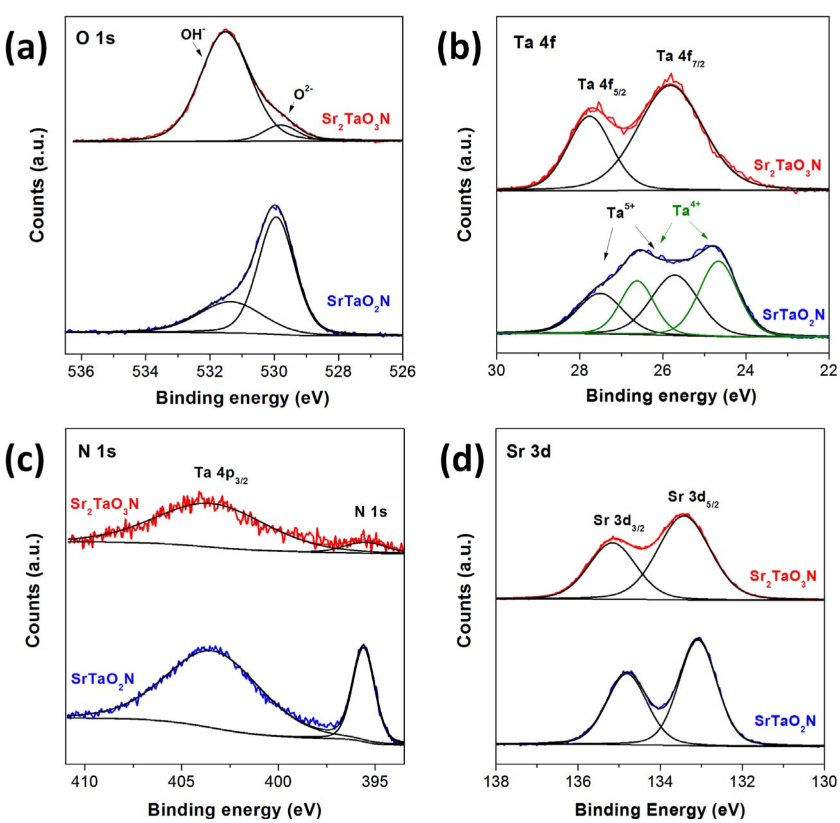

Fig. 5. XPS spectra of anions for $SrTaO_2N$ and Sr_2TaO_3N: (a) O 1*s*, (b) Ta 4*f*, (c) N 1*s* and (d) Sr 3*d*, respectively.

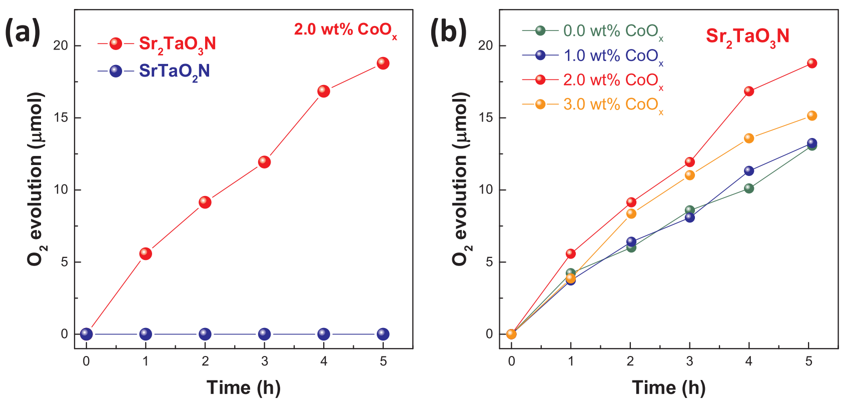

Fig. 6. (a) Temporal photocatalytic oxygen evolution for $SrTaO_2N$ and Sr_2TaO_3N loaded with 2.0wt% CoO_x under visible light illumination (λ ≥ 420 nm) and (b) temporal photocatalytic oxygen evolution for Sr_2TaO_3N loaded with different amounts of CoO_x cocatalyst. Experimental conditions: 50 mg sample powders and $AgNO_3$ (0.025 M) as sacrificial agent.

indiscernible oxygen production under visible light illumination for 5 h, confirming its poor photocatalytic activity for water oxidation. In the meantime, persistent N_2 signals was detected during the whole experimental period, suggesting that self-oxidative decomposition do occur at the surface of $SrTaO_2N$. On the contrary, continuous O_2 evolution was observed for Sr_2TaO_3N under the same experimental conditions, highlighting the effectiveness of structural lamination (inserting extra layers of SrO) in improving the photocatalytic performance. The improvements on photocatalytic performance can be further realized by the fact that Sr_2TaO_3N has a much smaller surface area than $SrTaO_2N$. More importantly, only trivial amounts of N_2 were released in the first hour for Sr_2TaO_3N, indicating a much improved stability compared to $SrTaO_2N$. As pointed out in the previous session, N in Sr_2TaO_3N is supposed to be more stable than the one in $SrTaO_2N$ as it has a higher electrostatic bond strength (2.55 vs 2.33) according to Pauling's second rule [59]. We have also attempted to optimize the photocatalytic activity of Sr_2TaO_3N by varying the amounts of cocatalyst CoO_x loaded. As can be seen in the Fig. 6b, 2 wt% CoO_x loading seems to give the highest activity among all loading points (0 wt%, 1 wt %, 2 wt% and 3 wt%). It is worth mentioning that loading CoO_x contributes to only small improvement on the activity and Sr_2TaO_3N is able to drive photocatalytic water oxidation reactions without the aid of a cocatalyst. More importantly, open-circuit voltage decay (OCVD) experiments clearly suggest better charge separation situations in Sr_2TaO_3N than $SrTaO_2N$ (Fig. S2). The electron lifetime in Sr_2TaO_3N is almost one order of magnitude higher than the one in $SrTaO_2N$, being responsible for the better photocatalytic activity for this laminated perovskite oxynitride. The stability of Sr_2TaO_3N has been confirmed by repeated use of the material for photocatalytic oxygen evolution as well as the same XRD patterns of the sample powders before and after the experiment (Figs. S3 and S4).

3.6. Band edge positions

We have then carried out Mott-Schottky analysis (MS) and XPS valence band scan on $SrTaO_2N$ and Sr_2TaO_3N with the aim to gain information on their band edge positions. Fig. 7a illustrates the MS plot of both samples. A positive MS slop can be seen for both $SrTaO_2N$ and Sr_2TaO_3N samples, suggesting that they are n-type semiconductors [81]. The flat-band potential (i.e. Fermi level) determined by extrapolating the linear part of MS curve down to the potential axis reads −0.45 V and −0.46 V (vs. NHE) for $SrTaO_2N$ and Sr_2TaO_3N, respectively, indicating that structural lamination has limited impact on the flat-band potential. In addition, XPS valence band scan reveals an energy gap of ~1.63 eV and ~1.80 eV between the valence band maximum (VBM) and the Fermi level for $SrTaO_2N$ and Sr_2TaO_3N, respectively (Fig. 7b). Recalling the band gap values determined by UV–vis absorption spectra (Fig. 4b), we can deduce the band edge positions for both samples and are schematically plotted in Fig. 7c. Both $SrTaO_2N$ and Sr_2TaO_3N demonstrate band edges straddling the redox potential of water, therefore, they are thermodynamically eligible for water splitting. The VBM of Sr_2TaO_3N is positively shifted by 0.16 V with regards to VBM of $SrTaO_2N$, being likely the reason for its higher photocatalytic activity and stability. The photo-generated holes in Sr_2TaO_3N are expected to have a larger over-potential for water oxidation than those in $SrTaO_2N$ and the self-decomposition is probably quenched due to the fast consumption of photo-generated holes.

3.7. Theoretical calculations

For better understanding the effect of structural lamination to the photocatalytic activity, we have performed theoretical calculations on the electronic structure of Sr_2TaO_3N. Fig. 8 illustrates the calculated band structures, total density of states (DOS) and projected density of states (PDOS) of all constituent elements in Sr_2TaO_3N. The semiconductivity of Sr_2TaO_3N is confirmed by a direct energy gap at **Γ** point as large as 1.22 eV in its band structures. This value is somewhat lower than the experimental value (~1.97 eV) determined by UV–vis spectra and is a common result of generalized gradient approximation (GGA) method that often underestimates the band gaps [82]. Nevertheless, the calculations give qualitative predictions. Close examinations on the band structures suggest that Sr_2TaO_3N has 2D charge transportation properties. This is verified by its anisotropic band dispersions along different crystallographic directions. Take valence band for example, band dispersions from **Γ** to **X** represents the hole behavior along (100) direction and covers a relatively large energy range (~1 eV). This implies that holes are facile to move along this direction as the effective mass of a carrier, m^*, is inversely proportional to the second derivative of E versus k curve (wide band leads to high mobility) (Eq. (2)) [83,84]:

$$m^* = \hbar^2 \left(\frac{d^2E}{dk^2} \right)^{-1} \tag{2}$$

However, band dispersions from **M** to **A** governs the hole behavior along (001) direction and are almost flat (nearly zero dispersions in energy), indicating that holes have an enormously large effective mass and are essentially forbidden to transport along this direction. Similar phenomena are also noticed in conduction band and charge effective mass is reasonably small along directions that perpendicular to (001) direction. Thereby, Sr_2TaO_3N has typical 2D charge transportation properties which probably arise from the insertion of extra layer of SrO and concomitant disconnection of TaO_4N_2 octahedron linkage. In addition, total density of states (DOS) and projected density of states (PDOS) suggest that conduction band minimum (CBM) is dominated by Ta 5d orbitals whilst valence band maximum (VBM) is constituted by the hybridization of N 2p and O 2p orbitals. Sr, thus serves merely as building blocks for the crystal structure of Sr_2TaO_3N and has negligible contribution to the electronic structures around Fermi level. Further projection of DOS to atomic orbitals reveals that N $2p_x/2p_y$ orbitals contribute mostly to the VBM and Ta $5d_{xy}$ orbitals dominates at CBM, respectively (Fig. 9). A more direct inspection of atomic orbital

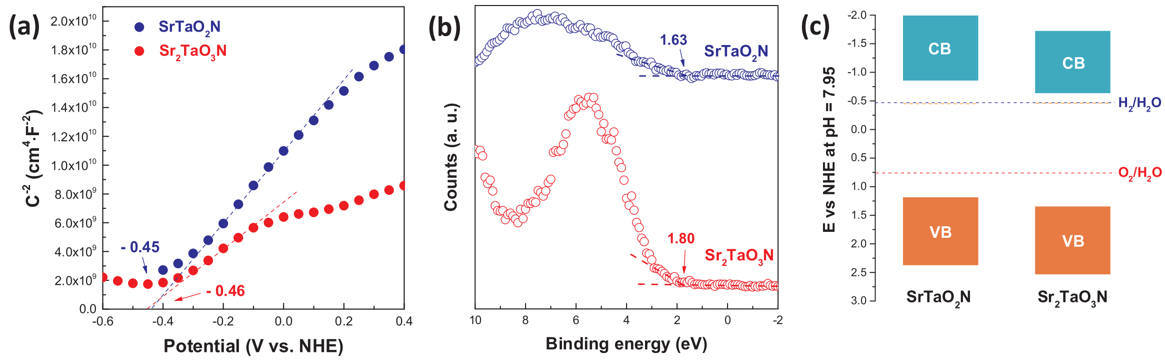

Fig. 7. Mott-Schottky plot (a), XPS valence band scan (b) and schematic representation of band edge positions at pH = 7.95 (c) of sample $SrTaO_2N$ and Sr_2TaO_3N, respectively. The capacitance data for Mott-Schottky analysis was extracted from impedance analysis at a fixed frequency of 1000 Hz and 10 mV amplitude.

contributions can be found in Fig. 10 which illustrates the density contour maps at VBM and CBM. The major contributions of N $2p_x/2p_y$ orbitals to CBM and dominant role of Ta $5d_{xy}$ orbitals to CBM can be clearly identified (Figs. 10 and S6). It is worth mentioning that only oxygen atoms at equatorial sites contribute slightly to VBM while those at apical sites have no contributions at all. Therefore, electrons and holes are confined in the TaN_2O_2 square planes which are well separated by two layers of SrO (Fig. 10). This result has important implications that charge recombination among different TaN_2O_2 square planes under light illumination is effectively prohibited and each TaN_2O_2 square plane acts as an independent photocatalyst. Structural lamination (i.e. inserting extra layers of SrO) from $SrTaO_2N$ to Sr_2TaO_3N thereby promotes the formation of these TaN_2O_2 square planes which favors efficient charge transportations, a similar case has been frequently found in copper-based superconductor which involves formation of CuO_4 square planes [85–87].

4. Conclusions

We have successfully laminated the crystal structure of $SrTaO_2N$ by inserting extra layers of SrO to form the Ruddlesden-Popper (RP) compound Sr_2TaO_3N. This structural modification substantially improves the optical properties of $SrTaO_2N$ by enhancing the short-wavelength photon absorption and extending absorption tail as far as 700 nm. A clear suppression of defects levels (e.g. Ta^{4+} etc.) is also noticed in Sr_2TaO_3N which probably arises from the inductive effect of Sr in enhancing the covalency of Ta−O(N) bond. More importantly, Sr_2TaO_3N is capable of photocatalytic water oxidation under visible light illumination without the aid of a cocatalyst and the self-oxidative decomposition is effectively suppressed. This is in striking contrast to $SrTaO_2N$ which has no photocatalytic activity and undergoes severe self-oxidative decomposition at the same conditions. The superior photocatalytic activity of Sr_2TaO_3N likely stems from the presence of extra SrO layers in the crystal structure which lower the VBM and stabilize N species according to Pauling's second rule. Theoretical calculations suggest that Sr_2TaO_3N has typical 2D charge transportation properties which are associated with the structural laminations. Electrons and holes in Sr_2TaO_3N are found to be confined within the TaN_2O_2 square planes which favors efficient charge transportations as charge recombination across different TaN_2O_2 square planes are essentially prohibited.

Acknowledgements

We thank Young Scientists Fund of the National Natural Science Foundation of China (Grant No. 21401142) for funding and Recruitment Program of Global Youth Experts (1000 plan). The work was supported by Shanghai Science and Technology Commission

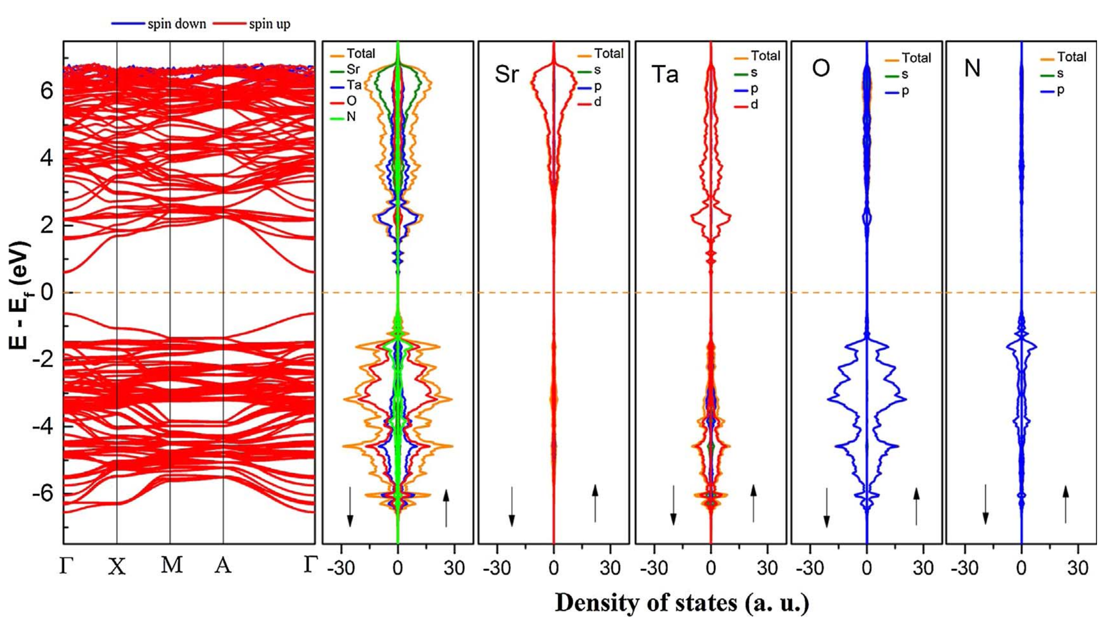

Fig. 8. Calculated band structure, total density of states (DOS) and projected density of states (PDOS) of all constituent elements in Sr_2TaO_3N, spin directions are indicated by arrows (↓↑) and the Fermi level is marked by dotted orange line. (For interpretation of the references to colour in this figure legend, the reader is referred to the web version of this article.)

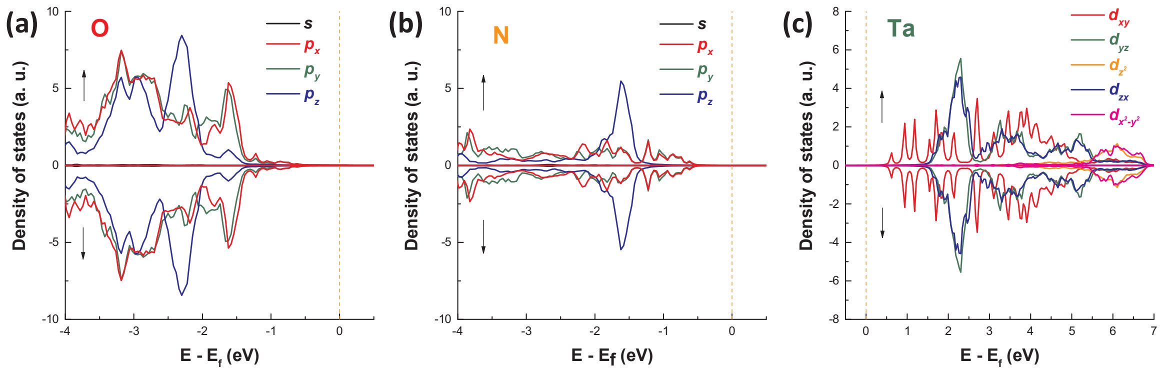

Fig. 9. Projected density of states of O 2p orbitals around VBM (a), N 2p orbitals around VBM (b) and Ta 5d orbitals around CBM (c), spin directions are indicated by arrows (↓↑) and the Fermi level is marked by dashed line.

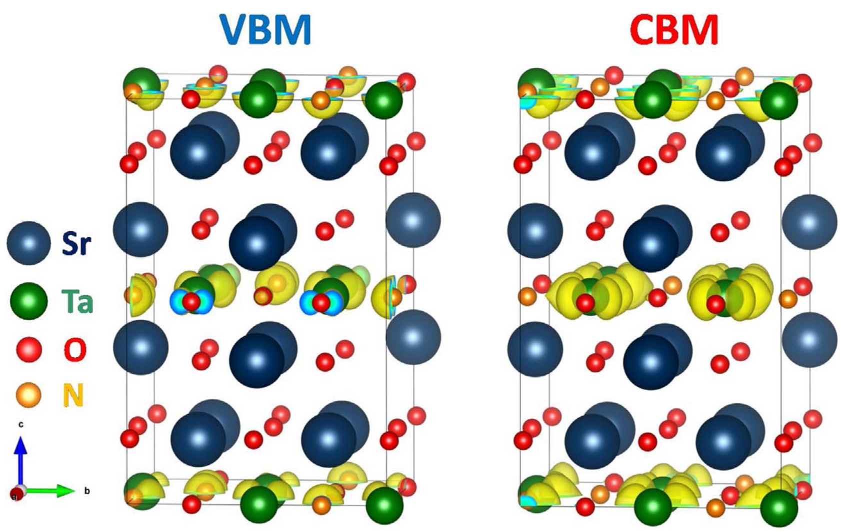

Fig. 10. Density contour maps of Sr_2TaO_3N at valence band maximum (VBM) and conduction band minimum (CBM), a 2 × 2 × 1 supercell (marked by black lines) is used for calculations.

(14DZ2261100) and the Fundamental Research Funds for the Central Universities.

Appendix A. Supplementary data

Supplementary material related to this article can be found, in the online version, at doi:https://doi.org/10.1016/j.apcatb.2018.01.071.

References

[1] Annual Energy Outlook 2017, U. S. Energy Information Administration, (2017).
[2] B. Dudley, BP Statistical Review of World Energy, June 2016 (2016).
[3] N.S. Lewis, D.G. Nocera, Powering the planet: chemical challenges in solar energy utilization, Proc. Natl. Acad. Sci. U. S. A. 103 (2006) 15729–15735.
[4] D.G. Nocera, Living healthy on a dying planet, Chem. Soc. Rev. 38 (2009) 13–15.
[5] J.A. Turner, A realizable renewable energy future, Science 285 (1999) 687–689.
[6] J.A. Turner, Sustainable hydrogen production, Science 305 (2004) 972–974.
[7] A. Fujishima, K. Honda, Electrochemical photolysis of water at a semiconductor electrode, Nature 238 (1972) 37–38.
[8] K. Maeda, K. Teramura, D.L. Lu, T. Takata, N. Saito, Y. Inoue, K. Domen, Photocatalyst releasing hydrogen from water – enhancing catalytic performance holds promise for hydrogen production by water splitting in sunlight, Nature 440 (2006) 295-295.
[9] F.T. Wagner, G.A. Somorjai, Photocatalytic hydrogen production from water on Pt-free SrTiO3 in alkali hydroxide solution, Nature 285 (1980) 559–560.
[10] Z.G. Zou, J.H. Ye, K. Sayama, H. Arakawa, Direct splitting of water under visible light irradiation with an oxide semiconductor photocatalyst, Nature 414 (2001) 625–627.
[11] Q. Wang, T. Hisatomi, Q.X. Jia, H. Tokudome, M. Zhong, C.Z. Wang, Z.H. Pan, T. Takata, M. Nakabayashi, N. Shibata, Y.B. Li, I.D. Sharp, A. Kudo, T. Yamada, K. Domen, Scalable water splitting on particulate photocatalyst sheets with a solar-to-hydrogen energy conversion efficiency exceeding 1%, Nat. Mater. 15 (2016) 611–615.
[12] X.C. Wang, K. Maeda, A. Thomas, K. Takanabe, G. Xin, J.M. Carlsson, K. Domen, M. Antonietti, A metal-free polymeric photocatalyst for hydrogen production from water under visible light, Nat. Mater. 8 (2009) 76–80.
[13] X.X. Xu, C. Randorn, P. Efstathiou, J.T.S. Irvine, A red metallic oxide photocatalyst, Nat. Mater. 11 (2012) 595–598.
[14] H.M. Chen, Y.H. Xie, X.Q. Sun, M.L. Lv, F.F. Wu, L. Zhang, L. Li, X.X. Xu, Efficient charge separation based on type-II g-C3N4/TiO2-B nanowire/tube heterostructure photocatalysts, Dalton Trans. 44 (2015) 13030–13039.
[15] H.M. Chen, X.Q. Sun, X.X. Xu, Ruddlesden-Popper compounds (SrO)(LaFeO3)n (n = 1 and 2) as p-type semiconductors for photocatalytic hydrogen production, Electrochim. Acta 252 (2017) 138–146.
[16] X.Q. Sun, Y.H. Xie, F.F. Wu, H.M. Chen, M.L. Lv, S. Ni, G. Liu, X.X. Xu, Photocatalytic hydrogen production over chromium doped layered perovskite Sr2TiO4, Inorg. Chem. 54 (2015) 7445–7453.
[17] M.L. Lv, S. Ni, Z. Wang, T.C. Cao, X.X. Xu, Cation ordering/disordering effects upon photocatalytic activity of CrNbO4, CrTaO4, Sr2CrNbO6 and Sr2CrTaO6, Int. J. Hydrogen Energy 41 (2016) 1550–1558.
[18] X.X. Xu, G. Liu, C. Randorn, J.T.S. Irvine, g-C3N4 coated SrTiO3 as an efficient photocatalyst for H2 production in aqueous solution under visible light irradiation, Int. J. Hydrogen Energy 36 (2011) 13501–13507.
[19] M.L. Lv, Y.W. Wang, L.W. Lu, R.N. Wang, S. Ni, G. Liu, X.X. Xu, Structural dependence of the photocatalytic properties of double perovsite compounds A2InTaO6 (A = Sr or Ba) doped with nickel, Phys. Chem. Chem. Phys. 18 (2016) 21491–21499.
[20] X.B. Chen, S.H. Shen, L.J. Guo, S.S. Mao, Semiconductor-based photocatalytic hydrogen generation, Chem. Rev. 110 (2010) 6503–6570.
[21] A. Kudo, Y. Miseki, Heterogeneous photocatalyst materials for water splitting, Chem. Soc. Rev. 38 (2009) 253–278.
[22] G. Zhang, G. Liu, L.Z. Wang, J.T.S. Irvine, Inorganic perovskite photocatalysts for solar energy utilization, Chem. Soc. Rev. 45 (2016) 5951–5984.
[23] F.F. Wu, G. Liu, X.X. Xu, Efficient photocatalytic oxygen production over Ca-modified LaTiO2N, J. Catal. 346 (2017) 10–20.
[24] Y.H. Xie, Y.W. Wang, Z.F. Chen, X.X. Xu, Role of oxygen defects on the photocatalytic properties of Mg-doped mesoporous Ta3N5, ChemSusChem 9 (2016) 1403–1412.
[25] F.F. Wu, M.L. Lv, X.Q. Sun, Y.H. Xie, H.M. Chen, S. Ni, G. Liu, X.X. Xu, Efficient photocatalytic oxygen production over nitrogen-doped Sr4Nb2O9 under visible-light irradiation, ChemCatChem 8 (2016) 615–623.

[26] F.F. Wu, X.Q. Sun, G. Liu, X.X. Xu, Actualizing efficient photocatalytic water oxidation over SrTaO2N by Na modification, Catal. Sci. Technol. 7 (2017) 4640–4647.
[27] Y.W. Wang, D.Z. Zhu, X.X. Xu, Zr-doped mesoporous Ta3N5 microspheres for efficient photocatalytic water oxidation, ACS Appl. Mater. Interfaces 8 (2016) 35407–35418.
[28] S. Balaz, S.H. Porter, P.M. Woodward, L.J. Brinson, Electronic structure of tantalum oxynitride perovskite photocatalysts, Chem. Mater. 25 (2013) 3337–3343.
[29] B. Siritanaratkul, K. Maeda, T. Hisatomi, K. Domen, Synthesis and photocatalytic activity of perovskite niobium oxynitrides with wide visible-light absorption bands, ChemSusChem 4 (2011) 74–78.
[30] Y. Moriya, T. Takata, K. Domen, Recent progress in the development of (oxy)nitride photocatalysts for water splitting under visible-light irradiation, Coord. Chem. Rev. 257 (2013) 1957–1969.
[31] M. Ahmed, X.X. Guo, A review of metal oxynitrides for photocatalysis, Inorg. Chem. Front. 3 (2016) 578–590.
[32] S.S.K. Ma, K. Maeda, T. Hisatomi, M. Tabata, A. Kudo, K. Domen, A redox-mediator-free solar-driven Z-scheme water-splitting system consisting of modified Ta3N5 as an oxygen-evolution photocatalyst, Chem.-Eur. J. 19 (2013) 7480–7486.
[33] S.S. Chen, S. Shen, G.J. Liu, Y. Qi, F.X. Zhang, C. Li, Interface engineering of a CoOx/Ta3N5 photocatalyst for unprecedented water oxidation performance under visible-light-irradiation, Angew. Chem. Int. Ed. 54 (2015) 3047–3051.
[34] M. Matsukawa, R. Ishikawa, T. Hisatomi, Y. Moriya, N. Shibata, J. Kubota, Y. Ikuhara, K. Domen, Enhancing photocatalytic activity of LaTiO2N by removal of surface reconstruction layer, Nano Lett. 14 (2014) 1038–1041.
[35] A. Kasahara, K. Nukumizu, T. Takata, J.N. Kondo, M. Hara, H. Kobayashi, K. Domen, LaTiO2N as a visible-light (< = 600 nm)-driven photocatalyst (2), J. Phys. Chem. B 107 (2003) 791–797.
[36] F. Oehler, S.G. Ebbinghaus, Photocatalytic Properties of CoOx-Loaded Nano-Crystalline Perovskite Oxynitrides ABO(2)N (A = Ca, Sr, Ba, La; B = Nb, Ta), Solid State Sci. 54 (2016) 43–48.
[37] M. Higashi, R. Abe, K. Teramura, T. Takata, B. Ohtani, K. Domen, Two step water splitting into H-2 and O-2 under visible light by ATaO(2)N (A = Ca, Sr, Ba) and WO3 with IO3-/I- shuttle redox mediator, Chem. Phys. Lett. 452 (2008) 120–123.
[38] M. Higashi, R. Abe, T. Takata, K. Domen, Photocatalytic overall water splitting under visible light using ATaO(2)N (A = Ca, Sr, Ba) and WO3 in a IO3-/I- shuttle redox mediated system, Chem. Mater. 21 (2009) 1543–1549.
[39] L. Zhang, Y. Song, J.Y. Feng, T. Fang, Y.J. Zhong, Z.S. Li, Z.G. Zou, Photoelectrochemical water oxidation of LaTaON2 under visible-light irradiation, Int. J. Hydrogen Energy 39 (2014) 7697–7704.
[40] S.J. Henderson, A.L. Hector, Structural and compositional variations in Ta3N5 produced by high-temperature ammonolysis of tantalum oxide, J. Solid State Chem. 179 (2006) 3518–3524.
[41] S. Khan, M.J.M. Zapata, M.B. Pereira, R.V. Goncalves, L. Strizik, J. Dupont, M.J.L. Santos, S.R. Teixeira, Structural, optical and photoelectrochemical characterizations of monoclinic Ta3N5 thin films, Phys. Chem. Chem. Phys. 17 (2015) 23952–23962.
[42] M. Hara, G. Hitoki, T. Takata, J.N. Kondo, H. Kobayashi, K. Domen, TaON and Ta3N5 as new visible light driven photocatalysts, Catal. Today 78 (2003) 555–560.
[43] Y.I. Kim, Y. Paik, M. Avdeev, Intercalation route to complex perovskites AM(0.2)Ta (0.8)O(2.8)N(0.2) (A = Sr, Bo; M = Li, Na): neutron diffraction and nuclear magnetic resonance study, Cryst. Growth Des. 15 (2015) 53–61.
[44] A.C. Larson, R.B. Von Dreele, GSAS-Generalised Crystal Structure Analysis System, Los Alamos National Laboratory Report No. LA-UR-86-748, (1994).
[45] P. Van der Heide, X-Ray Photoelectron Spectroscopy – An Introduction to Principles and Practices, John Wiley & Sons, Inc, Hoboken, New Jersey, 2012.
[46] G. Kresse, J. Furthmuller, Efficient iterative schemes for ab initio total-energy calculations using a plane-wave basis set, Phys. Rev. B 54 (1996) 11169–11186.
[47] J.P. Perdew, K. Burke, M. Ernzerhof, Generalized gradient approximation made simple, Phys. Rev. Lett. 77 (1996) 3865–3868.
[48] G. Kresse, D. Joubert, From ultrasoft pseudopotentials to the projector augmented-wave method, Phys. Rev. B 59 (1999) 1758–1775.
[49] H.J. Monkhorst, J.D. Pack, Special points for brillouin-zone integrations, Phys. Rev. B 13 (1976) 5188–5192.
[50] M.H. Yang, J. Oro-Sole, J.A. Rodgers, A.B. Jorge, A. Fuertes, J.P. Attfield, Anion order in perovskite oxynitrides, Nat. Chem. 3 (2011) 47–52.
[51] A. Fuertes, Metal oxynitrides as emerging materials with photocatalytic and electronic properties, Mater. Horiz. 2 (2015) 453–461.
[52] A. Fuertes, Chemistry and applications of oxynitride perovskites, J. Mater. Chem. 22 (2012) 3293–3299.
[53] M. Yang, J. Oro-Sole, A. Kusmartseva, A. Fuertes, J.P. Attfield, Electronic tuning of two metals and colossal magnetoresistances in EuWO1 + xN2-x perovskites, J. Am. Chem. Soc. 132 (2010) 4822–4829.
[54] A. Fuertes, Synthesis and properties of functional oxynitrides – from photocatalysts to CMR materials, Dalton Trans. 39 (2010) 5942–5948.
[55] L. Clark, J. Oro-Sole, K.S. Knight, A. Fuertes, J.P. Attfield, Thermally robust anion-chain order in oxynitride perovskites, Chem. Mater. 25 (2013) 5004–5011.
[56] E. Gunther, R. Hagenmayer, M. Jansen, Structural investigations on the oxidenitrides SrTaO2N, CaTaO2N and LaTaON2 by neutron and X-ray powder diffraction, Z. Anorg. Allg. Chem. 626 (2000) 1519–1525.
[57] Y.R. Zhang, T. Motohashi, Y. Masubuchi, S. Kikkawa, Local anionic ordering and anisotropic displacement in dielectric perovskite SrTaO2N, J. Ceram. Soc. Jpn. 119 (2011) 581–586.
[58] P. Barrie, T.A. Coffey, G.D. Forster, G. Hogarth, Bent vs. linear imido ligation at the octahedral molybdenum(VI) dithiocarbamate stabilised centre, J. Chem. Soc. Dalton (1999) 4519–4528.
[59] L. Pauling, The principles determining the structure of complex ionic crystals, J. Am. Chem. Soc. 51 (1929) 1010–1026.
[60] G. Tobias, D. Beltran-Porter, O.I. Lebedev, G. Van Tendeloo, J. Rodriguez-Carvajal, A. Fuertes, Anion ordering and defect structure in Ruddlesden-Popper strontium niobium oxynitrides, Inorg. Chem. 43 (2004) 8010–8017.
[61] N. Diot, R. Marchand, J. Haines, J.M. Leger, P. Macaudiere, S. Hull, Crystal structure determination of the oxynitride Sr2TaO3N, J. Solid State Chem. 146 (1999) 390–393.
[62] S.J. Clarke, K.A. Hardstone, C.W. Michie, M.J. Rosseinsky, High-temperature synthesis and structures of perovskite and n = 1 Ruddlesden-Popper tantalum oxynitrides, Chem. Mater. 14 (2002) 2664–2669.
[63] A. Kasahara, K. Nukumizu, G. Hitoki, T. Takata, J.N. Kondo, M. Hara, H. Kobayashi, K. Domen, Photoreactions on LaTiO2N under visible light irradiation, J. Phys. Chem. A 106 (2002) 6750–6753.
[64] J. Etourneau, J. Portier, F. Menil, The role of the inductive effect in solid state chemistry: how the chemist can use it to modify both the structural and the physical properties of the materials, J. Alloy Compd. 188 (1992) 1–7.
[65] C.E. Housecroft, A.G. Sharpe, Inorganic Chemistry, third edition, Pearson Education Limited, England, 2008.
[66] L.W. Lu, M.L. Lv, G. Liu, X.X. Xu, Photocatalytic hydrogen production over solid solutions between BiFeO3 and SrTiO3, Appl. Surf. Sci. 391 (2017) 535–541.
[67] L. Jiang, S. Ni, G. Liu, X.X. Xu, Photocatalytic hydrogen production over Aurivillius compound Bi3TiNbO9 and its modifications by Cr/Nb co-doping, Appl. Catal. B-Environ. 217 (2017) 342–352.
[68] L.W. Lu, S. Ni, G. Liu, X.X. Xu, Structural dependence of photocatalytic hydrogen production over La/Cr co-doped perovskite compound ATiO3 (A = Ca, Sr and Ba), Int. J. Hydrogen Energy 42 (2017) 23539–23547.
[69] M.L. Lv, G. Liu, X.X. Xu, Homologous compounds ZnnIn2O3 + n (n = 4, 5 and 7) containing laminated functional groups as efficient photocatalyt for hydrogen production, ACS Appl. Mater. Interfaces 8 (2016) 28700–28708.
[70] M.L. Lv, Y.H. Xie, Y.W. Wang, X.Q. Sun, F.F. Wu, H.M. Chen, S.W. Wang, C. Shen, Z.F. Chen, S. Ni, G. Liu, X.X. Xu, Bismuth and chromium co-doped strontium titanates and their photocatalytic properties under visible light irradiation, Phys. Chem. Chem. Phys. 17 (2015) 26320–26329.
[71] X.Q. Sun, S.W. Wang, C. Shen, X.X. Xu, Efficient photocatalytic hydrogen production over Rh-doped inverse spinel Zn2TiO4, ChemCatChem 8 (2016) 2289–2295.
[72] S. Selcuk, A. Selloni, Facet-dependent trapping and dynamics of excess electrons at anatase TiO2 surfaces and aqueous interfaces, Nat. Mater. 15 (2016) 1107-+.
[73] H. Hussain, G. Tocci, T. Woolcot, X. Torrelles, C.L. Pang, D.S. Humphrey, C.M. Yim, D.C. Grinter, G. Cabailh, O. Bikondoa, R. Lindsay, J. Zegenhagen, A. Michaelides, G. Thornton, Structure of a model TiO2 photocatalytic interface, Nat. Mater. 16 (2017) 461-+..
[74] S.J. Tan, H. Feng, Y.F. Ji, Y. Wang, J. Zhao, A.D. Zhao, B. Wang, Y. Luo, J.L. Yang, J.G. Hou, Observation of photocatalytic dissociation of water on terminal Ti sites of TiO2(110)-1 x 1 surface, J. Am. Chem. Soc. 134 (2012) 9978–9985.
[75] R. Wang, K. Hashimoto, A. Fujishima, M. Chikuni, E. Kojima, A. Kitamura, M. Shimohigoshi, T. Watanabe, Light-induced amphiphilic surfaces, Nature 388 (1997) 431–432.
[76] M.V. Ivanov, T.V. Perevalov, V.S. Aliev, V.A. Gritsenko, V.V. Kaichev, Electronic structure of delta-Ta2O5 with oxygen vacancy: ab initio calculations and comparison with experiment, J. Appl. Phys. 110 (2011).
[77] X. Yu, W. Li, Z.H. Li, J.W. Liu, P.A. Hu, Defect engineered Ta2O5 nanorod: one-pot synthesis, visible-light driven hydrogen generation and mechanism, Appl. Catal. B-Environ. 217 (2017) 48–56.
[78] S.S. Chen, J.X. Yang, C.M. Ding, R.G. Li, S.Q. Jin, D.E. Wang, H.X. Han, F.X. Zhang, C. Li, Nitrogen-doped layered oxide Sr5Ta4O15-xNx for water reduction and oxidation under visible light irradiation, J. Mater. Chem. A 1 (2013) 5651–5659.
[79] K. Ohbayashi, K. Yoshida, M. Anma, Y. Takai, H. Hayakawa, Bismuth valence studies of as-grown superconducting Bi-Sr-Ca-Cu-O thin-films with Tc(zero) from 98-K to 66-K, Jpn. J. Appl. Phys. 2 (31) (1992) L953–L955.
[80] Y.J. Zhong, Z.S. Li, X. Zhao, T. Fang, H.T. Huang, Q.F. Qian, X.F. Chang, P. Wang, S.C. Yan, Z.T. Yu, Z.G. Zou, Enhanced water-splitting performance of perovskite SrTaO2N photoanode film through ameliorating interparticle charge transport, Adv. Funct. Mater. 26 (2016) 7156–7163.
[81] K. Gelderman, L. Lee, S.W. Donne, Flat-band potential of a semiconductor: using the Mott-Schottky equation, J. Chem. Educ. 84 (2007) 685–688.
[82] H. Xiao, J. Tahir-Kheli, W.A. Goddard, Accurate band gaps for semiconductors from density functional theory, J. Phys. Chem. Lett. 2 (2011) 212–217.
[83] C. Kittel, Introduction to Solid State Physics, 7th ed., Wiley, New York, 1996.
[84] H. Mizoguchi, P.M. Woodward, Electronic structure studies of main group oxides possessing edge-sharing octahedra: implications for the design of transparent conducting oxides, Chem. Mater. 16 (2004) 5233–5248.
[85] J.G. Bednorz, K.A. Muller, Possible high-Tc superconductivity in the Ba-La-Cu-O system, Z. Phys. B Condens. Matter 64 (1986) 189–193.
[86] V. Manivannan, J. Gopalakrishnan, Synthesis of cuprates of perovskite structure in the Ba-Pb-Cu-O, Ba-Bi-Cu-O, and Ba-Pb-Tl-Cu-O systems – possible high-Tc superconductivity in a perovskite-like phase in the Ba-Pb-Tl-Cu-O system (Vol 109, Pg 205, 1994), J. Solid State Chem. 111 (1994) 448-448.
[87] M.K. Wu, J.R. Ashburn, C.J. Torng, P.H. Hor, R.L. Meng, L. Gao, Z.J. Huang, Y.Q. Wang, C.W. Chu, Superconductivity at 93-K in a new mixed-phase Y-Ba-Cu-O compound system at ambient pressure, Phys. Rev. Lett. 58 (1987) 908–910.